# Nanoscale

Accepted Manuscript


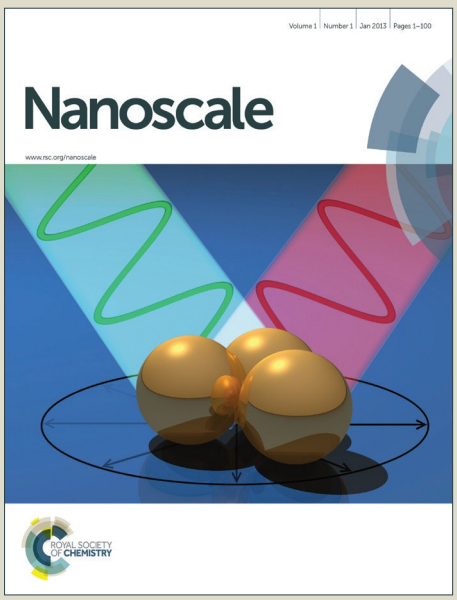





ROYAL SOCIETY OF CHEMISTRY

www.rsc.org/nanoscale

Cite this: DOI: 10.1039/c0xx00000x

www.rsc.org/xxxxxx

ARTICLE TYPE

# Biochemistry-Directed Hollow Porous Microspheres: Bottom-Up Self-Assembled Polyanion-based Cathodes for Sodium Ion Batteries

**Bo Lin[a], Qiufeng Li[b], Baodong Liu[c], Sen Zhang*[,b], Chao Deng*[,a]**

***Received (in XXX, XXX) Xth XXXXXXXXX 20XX, Accepted Xth XXXXXXXXX 20XX***
**DOI: 10.1039/b000000x**

Biochemistry-directed synthesis of functional nanomaterials has attracted great interests in energy storage, catalysis and other applications. The unique ability of biological systems to guide molecule self-assembling facilitates the construction of distinctive architectures with desirable physicochemical characteristics. Herein, we report a biochemistry-directed "bottom-up" approach to construct hollow porous microspheres of polyanion materials for sodium ion battery. Two kinds of polyanions, *i.e.* $Na_3V_2(PO_4)_3$ and $Na_{3.12}Fe_{2.44}(P_2O_7)_2$, are employed as cases in this study. The microalgae cell realizes the formation of spherical "bottom" bio-precursor. Its tiny core is subjected to destroy and tough shell tends to carbonize upon calcination, resulting in the hollow porous microspheres for the "top" product. The nanoscale crystals of the polyanion materials are tightly enwrapped by the highly-conductive framework in the hollow microsphere, resulting in the hierarchical nano-microstructure. The whole formation process is disclosed as a "bottom-up" mechanism. Moreover, the biochemistry-directed self-assembly process is confirmed to play a crucial role in the construction of the final architecture. Taking advantage of the well-defined hollow-microsphere architecture, the abundant interior voids and the highly-conductive framework, the polyanion materials show favourable sodium-intercalation kinetics. Both materials are capable of high-rate long-term cycling. After five hundred cycles at 20 *C* and 10 *C*, $Na_3V_2(PO_4)_3$ and $Na_{3.12}Fe_{2.44}(P_2O_7)_2$ retain 96.2% and 93.1% of the initial capacity, respectively. Therefore, the biochemistry-directed technique provides a low-cost, highly-efficient and wide-applicable strategy to produce high-performance polyanion-based cathodes for sodium ion battery.

KEYWORDS: biochemistry-directed strategy; bottom-up; polyanion composite; energy storage device

## 1 Introduction

Concerns over global energy supply and climate-change have promoted intensive research on energy storage technologies. Rechargeable batteries with high storage capacity and cycling stability are considered to be the versatile, clean and promising energy storage systems.[1] Among present rechargeable batteries, lithium ion batteries (LIBs) have the highest energy density. However, the high cost of lithium highly motivates both academia and industry to develop cheap and safe battery technologies.[2] Recently, sodium ion batteries (SIBs) have attracted great attention because of the abundant resource, low cost of sodium and similar chemistry to lithium.[3,4] However, the larger radium of sodium in comparison to lithium leads to the low ion insertion reversibility, inferior kinetics and phase instability of the sodium hosts.[5-8] Therefore, it is imperative to create high-performance sodium-ion electrode materials with fast kinetics and good stability to realize the full potential of NIBs.

Tailoring electroactive materials into diverse specialized architecture are triggering unprecedented innovations. Tremendous efforts have been made to fabricate novel architectures to improve the properties of electrode materials. The 3D hollow and/or porous architectures show great superiority.[9-15] Its abundant interior voids enable easy electrolyte penetration and the hierarchical porosity alleviates volume change during ion de/intercalation. Thus it is an ideal architecture for electrode materials. Many oxides (*e.g.* $VO_2$, $MoO_3$, $TiO_2$)[9-12] and simple inorganic composites (*e. g.* carbon, Si)[13-15] have been constructed with this architecture and applied in the electrochemical systems. However, its application with more complex polyanion-based sodium host is still challenging and remains largely unexplored. Therefore, it is significant to find an efficient strategy to tailor such architecture for polyanion-based materials. It is especially important for those in sodium system, which has intrinsically inferior kinetics and phase instability.

In nature, diverse organisms display a dazzling variety of one-, two- and three-dimensional structures from nano- to millimeter length scales.[16-20] The cheap, abundant and renewable biological organisms promote scientists to open a new intercross subject between the biology, chemistry and materials engineering. The biochemistry-directed technique uses the biological toolkit to direct the self-assembling of materials and produces additional functionality. Various biological organisms such as DNA,[17] virtus,[18] cells,[19] plants,[20] *et al.* have been employed as

biotemplates. Many nanostructured materials, including oxides (*e.g.* NiO, $Fe_2O_3$, CuO, MnO),[21,22] metals (*e.g.* Au)[23], simple inorganic materials (*e.g.* C, Sn)[24,25] and phosphates (*e.g.* $FePO_4$)[19] have been successfully produced.

The electrode materials prepared by bio-directed technique show superiority in rechargeable batteries, especially the lithium and sodium ions batteries.[21-27] Various bio-inspired cathodes have been constructed and achieved excellent electrochemical performance. Xia *et al.*[26] prepared the nano-$LiFePO_4$/C based on spirulina biotemplate, which showed remarkable capacity and excellent cycling stability in lithium ion batteries. Moradi *et al.*[19] prepared a M13 viruses-templated $FePO_4$/SWCNTs composite and achieved a high discharge capacity of 166 mAh $g^{-1}$ in sodium ion battery. Zhou *et al.*[27] used recombinant ELP16 proteins as biotemplate to prepare $Li_3V_2(PO_4)_3$ and $Na_3V_2(PO_4)_3$/C composites and achieved ultrafast rate capabilities and excellent cycle performance in both lithium and sodium batteries. The superior electrochemical performance of these bio-inspired cathodes demonstrate the high-efficiency of biochemistry technique in energy storage devices.

Microalgae are a special category in the nature. *Nannochloropsis oculata* (abbreviated as *N. oculata*) is a single cell biological organism possesses spherical shape and microscale diameter (1~4 μm). The fast growth rate and easily cultivation result in the huge production of more than twenty tons per hectare per year.[28] Thus it is a cheap, abundant and green resource in nature. The high biological activity and good accumulation ability facilitate the adsorption and grasp of heavy metal ions, and guide the self-assembling of functional materials.[29,30] Moreover, the carbohydrate in the cell shell can serve as a natural carbon source to construct carbon-based framework in porous architecture. Therefore, it is a good biotemplate for high-performance electrode materials.

Inspired by these advantages, we report the construction of hollow porous microspheres for polyanion-based sodium hosts *via* a microalgae-based biochemistry-directed bottom-up strategy. Two polyanions of $Na_3V_2(PO_4)_3$ and $Na_{3.12}Fe_{2.44}(P_2O_7)_2$ are chose as model materials. Moreover, this strategy can also be applied to other polyanions as well. Each prepared microball possesses a carbon-based framework and hollow porous architecture. When applied in sodium ion system, it exhibits superior sodium diffusion capability and excellent cycling stability, which demonstrates the superiority of biochemistry-directed technique in energy storage devices.

## 2 Experimental

### *2.1 Synthesis*

**Microalgae cultivation.** *N. oculata* cells were obtained from Marine Biological Culture Center (Qingdao, China). They were screened for purification and stored at 5~10 °C. When cultivation began, the microalgae cells were transferred to sterile conical flasks with f/2 medium and artificial seawater (Qingdao, China). Then the flasks were placed in an artificial environmental box (Jumbo LRH-250-G3, Guangdong, China). The growth was at the stationary conditions: temperature of 24±1 °C, light intensity of 200 μ mol $m^{-2}$ $s^{-1}$ and ratio of light to dark is 12:12. Steady shaking was carried out three times a day to ensure the equal growth. After 15~20 days, the cells were harvested. The obtained cells were washed and centrifuged five times in the deionized water to remove unwanted impurities. Finally, the purified and concentrated cells were collected for further use.

**Preparation of $Na_3V_2(PO_4)_3$/$Na_{3.12}Fe_{2.44}(P_2O_7)_2$ precursor.** The precursors of $Na_3V_2(PO_4)_3$ and $Na_{3.12}Fe_{2.44}(P_2O_7)_2$ were prepared by sol-gel process. For $Na_3V_2(PO_4)_3$, stoichiometric amount of $Na_2CO_3$, $NH_4H_2PO_4$, $NH_4VO_3$ and desirable citric acid were dissolved into distilled water under vigorous stirring. Then the mixture was transferred to a water bath at 80 °C under continuously stirring for six hours. The obtained concentrated transparent solution was the precursor solution of $Na_3V_2(PO_4)_3$. For $Na_{3.12}Fe_{2.44}(P_2O_7)_2$, iron powder was dissolved into citric acid solution under vigorously stirring until a clear sol was formed. Then the mixture of $Na_2CO_3$ and $NH_4H_2PO_4$ were added into above solution, and it was transferred to a water bath at 80 °C under vigorous stirring for six hours. The obtained concentrated transparent solution was the precursor solution of $Na_{3.12}Fe_{2.44}(P_2O_7)_2$.

**Construction of $Na_3V_2(PO_4)_3$/$Na_{3.12}Fe_{2.44}(P_2O_7)_2$ 3D hollow porous microballs and reference samples.** The $Na_3V_2(PO_4)_3$ and $Na_{3.12}Fe_{2.44}(P_2O_7)_2$ precursor solutions were cooled at room temperature. Then 20 mL concentrated microalgae cells solution was dropped into the precursor solutions under magnetic stirring. The mixtures were firstly stayed at room temperature for two hours, and then elevated to 50 °C for three hours. Next, the suspension was centrifuged and dried to achieve the bio-precursor. Finally, the resultant powders were annealed at 750 and 600 °C respectively for 8 hours at flowing argon atmosphere to achieve the $Na_3V_2(PO_4)_3$ and $Na_{3.12}Fe_{2.44}(P_2O_7)_2$ hollow microspheres.

**Preparation of reference samples.** For comparison, two reference samples were prepared via conventional sol-gel synthesis (Supplementary S1).

### *2.2 Materials characterization*

Powder X-ray diffraction (XRD, Bruker D8/Germany) using Cu Kα radiation was employed to identify the crystalline phase of the material. The experiment was performed by using step mode with a fixed time of 3 *s* and a step size of 0.02°. The XRD pattern was refined by using the Rietveld method. The morphology was observed with a scanning electron microscope (SEM, HITACHIS-4700) and a transmission electron microscope (TEM, JEOS-2010 PHILIPS). Raman spectra were recorded with a Labram HR-800 (HORIBA JobinYvon) spectrometer. Nitrogen adsorption-desorption isotherms were measured using a Micromeritics ASAP 2010 sorptometer and specific surface area and pore size distribution were calculated correspondingly. Carbon contents of the samples were determined by an element analyzer (EA, Elementar Vario EL).

### *2.3 Electrochemical measurements*

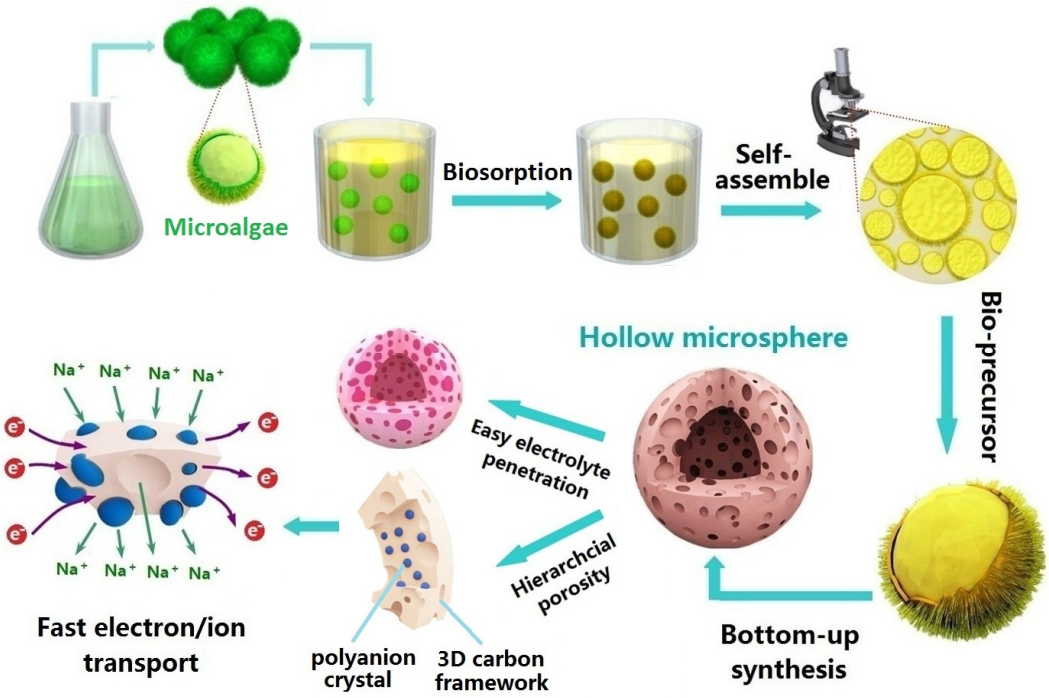


Figure 1 Schema of the biochemistry-directed synthesis of the hollow porous microspheres for polyanion composites. The preparation process of the "bottom" bio-precursor and the "up" polyanion product are emphasized. The partially enlarged image emphasizes the hierarchical porosity and nanoparticles enwrapped in the carbon-based framework. The high-efficiency electrolyte penetration and fast electron/ion transport pathways in the hollow porous microspheres are illustrated.

The electrochemical characteristics were measured in CR2032 coin cells. The coin cells were assembled in an argon filled glove box. Each composite electrode was made from a mixture of the active material, carbon black and polyvinylidene fluoride (PVDF) in a weight ratio of 8:1:1. Na foil was employed as counter and reference electrode and 1 $mol \cdot L^{-1}$ $NaClO_4$ dissolved in propylene carbonate (PC) was used as electrolyte. For the galvanostatic intermittent titration technique (GITT), a constant current of 0.05 C was applied for 10 min and then interrupted to open circuit condition for 60 min. This process was repeated until the cathode potential exceeded the cut-off potential. Galvanostatic charge-discharge tests were performed on a Land battery testing system (Wuhan, China). EIS measurements were conducted using a Zivelab electrochemical workstation, and the applied frequency range is 100k~5 mHz.

## 3 Results and Discussion

### 3.1 Biochemistry-directed strategy

The construction of 3D hollow porous microspheres for $Na_3V_2(PO_4)_3$ and $Na_{3.12}Fe_{2.44}(P_2O_7)_2$ composites proceeds along a bottom-up approach (Figure 1). Firstly, the biotemplates of microalgae cells were purified and dropped into the precursor solutions. Then, the bio-prepcursors are prepared through a biosorption and self-assembling process. The high bio-activity enables the microalgae cells to capture guest metal ions.[22,25-30] Moreover, the superior liquid accumulation and highly-efficient solution impregnation ensure the cells to well adsorb the precursor solutions.[25-30] Both results in the well-defined spherical morphology and uniform composition of the "bottom" bio-precursors. In the following calcination process, the microalgae cells and the organic groups in bio-precursors are decomposed to carbon-based framework. Simultaneously, the polyanion crystals are formed, and the final "up" product of polyanion-based hollow microsphere is constructed. The whole biochemistry-directed process is low-cost, easy handling and energy saving, which shows great superiority to traditional artificial methods.[9-15,31,32]

Moreover, the well-defined architecture derived from microalgae biotemplate is beneficial to sodium intercalation. As illustrated in Figure 1, the $Na_3V_2(PO_4)_3$ and $Na_{3.12}Fe_{2.44}(P_2O_7)_2$ crystals are enwrapped in the carbon shell, which construct the framework of hollow porous microballs. The carbon-based three-dimensional conductive framework ensures the fast electron transport; and the abundant interior voids facilitate easy electrolyte penetration and fast ion transport. Moreover, the hierarchical porosity alleviates crystal volume change, which is beneficial to its structure integrity during sodium de/intercalation. Therefore, the hollow porous spherical structure is favorable to both fast kinetics and stable cycling of the electrode materials for sodium ion batteries.

### 3.2 Hollow porous microsphere for polyanion-based sodium hosts

The morphology and microstructure of the $Na_3V_2(PO_4)_3$ and $Na_{3.12}Fe_{2.44}(P_2O_7)_2$ microballs are investigated by SEM and TEM observations. As displayed in Figure 2 (a, b), both composites have spherical particles with the diameters of 2~3 μm. The

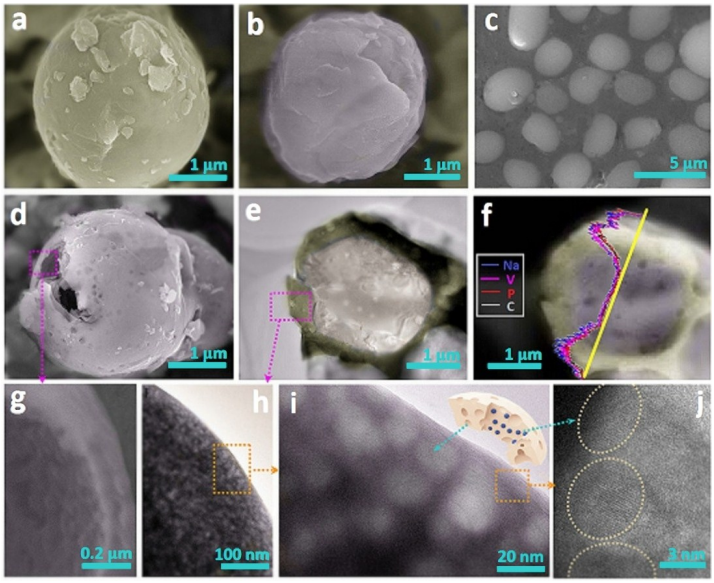


Figure 2 Morphologies and microstructures of the hollow porous microspheres: SEM images of the $Na_{3.12}Fe_{2.44}(P_2O_7)_2$ (a) and $Na_3V_2(PO_4)_3$ (b) microspheres; (c) Low-resolution SEM image of the hollow porous microballs; SEM (d) and TEM (e) images of one cracked hollow microball; (f) Bright-field TEM and EDS-STEM line-scan of the hollow microball; (g, h, i) partially enlarged images of the shell filled with hierarchical pores; (j) HRTEM image of the framework for the hollow microsphere as emphasized in the square of i. The schematic architecture of a partially disclosed shell in the microsphere is displayed as inset of i.

uniform size and morphology observed in the low-magnification image (Figure 2c) demonstrate the successful construction of microspheres through copying *N. oculata* biotemplate. The cross-section images demonstrate the hollow feature inside the microspheres (Figure 2d, e, g). As displayed in Figure 2e~i, the microspheres have one big void in the core (Figure 2e, f) and abundant small pores on the shell (Figure 2g~i). Moreover, the enlarged image of the shell further demonstrate the interconnections between the pores, which provide even smaller pores on the shells (Figure 2h, i). The hierarchical porous architecture is also evidenced by the multiple porosities in the pore size distribution analysis (Figure s1). Therefore, two major features of the biochemistry-directed microsphere, *i.e.* the hollow microspherical framework and the hierarchical porous architecture, are favorable to easy electrolyte penetration and promote fast ion transport.

More complete understanding of the hollow microspheres is provided by EDS-STEM results and high-resolution TEM observation. As displayed in Figure 2f, all of the elements have similar tendency in the line-scan element mapping, which is agreed with the bright-field TEM image. The result verifies the uniform composition and hollow structure of the microspheres. Moreover, the HRTEM observation clarifies the detailed architecture of the shell. As displayed in Figure 2j, the designed regions with lattice fringes certify the nanocrystals of polyanions, and the outside parts without lattice fringes demonstrate the amorphous carbon network. Therefore, as schematically illustrated in the inset of Figure 2i, the shell is composed of the amorphous carbon-based network, which enwraps the nanoscale ployanion particles. The lattice fringes of the nanocrystals have an interplanar distance of 0.617 nm, corresponding to the (012) lattice planes of the polyanion phase, *i.e.* $Na_3V_2(PO_4)_3$ in this case. Same structure is also obtained for the $Na_{3.12}Fe_{2.44}(P_2O_7)_2$ phase (Figure s2). Thus the results demonstrate the single crystal nature of the nanoscale particles. The carbon shell not only provides continuous pathways for fast electron transport, but also modifies the surface state of the nanoparticles. Therefore, above results demonstrate that the hollow porous microspheres with 3D conductive framework and nanoscale particles have been successfully constructed for both polyanion-based composites through biochemistry-directed strategy.

The crystal structures of both bio-directed composites are identified by X-ray diffraction (XRD). The materials prepared via conventional sol-gel strategy are also employed as reference samples. The morphological and physical characteristics of the reference samples are displayed in Figure s3. The carbon contents of the bioinspired $Na_3V_2(PO_4)_3$ and $Na_{3.12}Fe_{2.44}(P_2O_7)_2$ samples are 5.1 wt.% and 5.4 wt%, respectively. As shown in Figure s3, the carbon content of each reference sample is similar to that of the corresponding bioinspired sample. As compared in Figure 3 (b and e), the lower surface area of the reference samples than the bio-directed ones is associated with their irregular microsized particles and low porosity. XRD patterns of the bio-directed and reference samples for both polyanion composites are displayed in Figure 3a and d. All the diffraction peaks of the $Na_3V_2(PO_4)_3$ composites can be indexed to the NASICON structure with $R\bar{3}c$ space group and those of the $Na_{3.12}Fe_{2.44}(P_2O_7)_2$ composites can be indexed to the triclinic structure with *P-1* space group. The absence of impurity phase indicates the high purity of all the materials. The wide broad backgrounds in the range of $20^o$~$40^o$ observed for the bio-directed samples are associated with

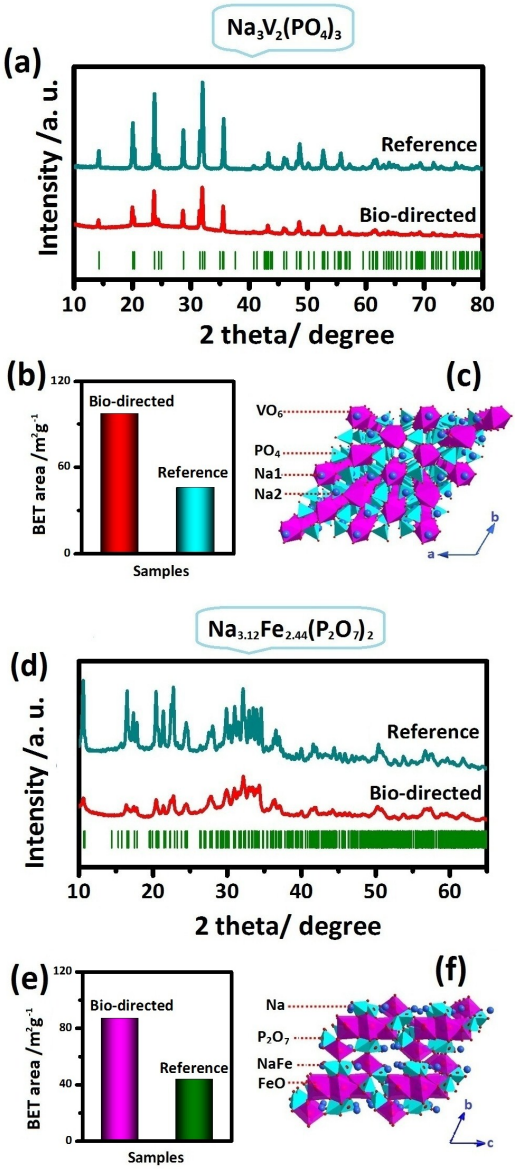


Figure 3 XRD patterns (a, d), BET areas (b, e) and crystal structure (c, f) of the bio-directed and reference samples for the $Na_3V_2(PO_4)_3$ (a, b, c) and $Na_{3.12}Fe_{2.44}(P_2O_7)_2$ (d, e, f) polyanion-based composites. Bragg diffraction positions (green ticks) of the $Na_3V_2(PO_4)_3$ and $Na_{3.12}Fe_{2.44}(P_2O_7)_2$ phases are displayed as inert of a and d.

the carbon matrix in these composites. The bio-directed samples exhibit lower peak densities than the references ones, which indicate their inferior crystallization. It can be attributed to the high porous structure and small crystals in the bio-directed microspheres as discussed above. The lattice parameters of all the samples are calculated by Rietveld refinements. As listed in table s1, the calculated parameters coincide well with previous report values.[31-33] Moreover, the element analysis results also demonstrate the ratios of Na/V and Na/Fe are well agreed with the designed value (Table s2). Combined above results, it confirms that desirable single-phase structure, uniform composition and well-defined hollow porous architecture have been successfully synthesized for both polyanion composites *via* the biochemistry-directed strategy.

On the other hand, Figure 3c and f illustrate the crystal structures of $Na_3V_2(PO_4)_3$ and $Na_{3.12}Fe_{2.44}(P_2O_7)_2$. For $Na_3V_2(PO_4)_3$, the basic unit of $[V_2(PO_4)_3]$ framework is constructed by two $VO_6$ octahedron and three $PO_4$ tetrahedra via corners sharing and sodium ions fully occupy the interstitial sites. For $Na_{3.12}Fe_{2.44}(P_2O_7)_2$, two $FeO_6$ octahedra and two $P_2O_7$ groups construct the crown unit of $Fe_2P_4O_{22}$ and $Fe_2P_4O_{20}$, which construct the basic unit of $Na_{3.12}Fe_{2.44}(P_2O_7)_2$ through corner sharing. The three-dimensional framework of both polyanion-based materials provides large interstitial spaces for sodium accommodation and offers channels for ion transport. Therefore, they are good cathode candidates for sodium ion batteries.

## 3.3 Formation mechanism of polyanion-based hollow microsphere

The biochemistry-directed approach is identified as an efficient route to build hollow porous microsphere for polyanion-based sodium hosts. Thus it is necessary to uncover the underlying mechanism, which guarantees the effectiveness of this approach. A possible formation mechanism of polyanion hollow porous microsphere is proposed.

Firstly, the spherical microalgae cell is employed as bio-template (Figure 4a). As illustrated in Figure 4l, the biological cell is composed of the polysaccharides-based shell and the lipid-based core. Besides the main elements of C and O, some elements from nutrition medium such as Ca, Mg and Si are also detected in the pristine microalgae cell (Figure 4i). Moreover, no heavy elements in the polyanion-based composite are detected in the biological organism (Figure 4e). Secondly, the microalgae cell is immerged into the precursor solutions. Its carboxyl groups tend to bind the heavy metal ions and the polysaccharides facilitate the element sequestrations[22,25,26]. Therefore, the cations in the precursor solutions are well absorbed by the microalgae. As evidenced by the EDS results, the elements of Na, V and P appear after cell biosorption process (Figure 4j). The uniform distribution of vanadium element demonstrates the homogenous solution absorption and uniform composition in the bio-precursor (Figure 4f). Moreover, the biosorption process doesn't destroy the structure of the cell (Figure 4b). Therefore, the "bottom" bio-precursor with well-defined spherical structure and uniform composition has been constructed.

Next, the spherical bio-precursor is high-temperature treated and the "up" product of hollow porous microsphere is produced (Figure 4c, d, g). The successful construction of the unique architecture is associated with the natural feature of microalgae cell. In nature, the core of biological cell is vulnerable and easy to destroy, while the shell is tough and able to resist outside damage (Figure 4l).[22,26,28-30] Therefore, the core of the cell is subject to be destroyed during heat treatment, and the cell shell tends to carbonize into porous framework. Meanwhile, the polyanion nanocrystals are also formed during the calcination

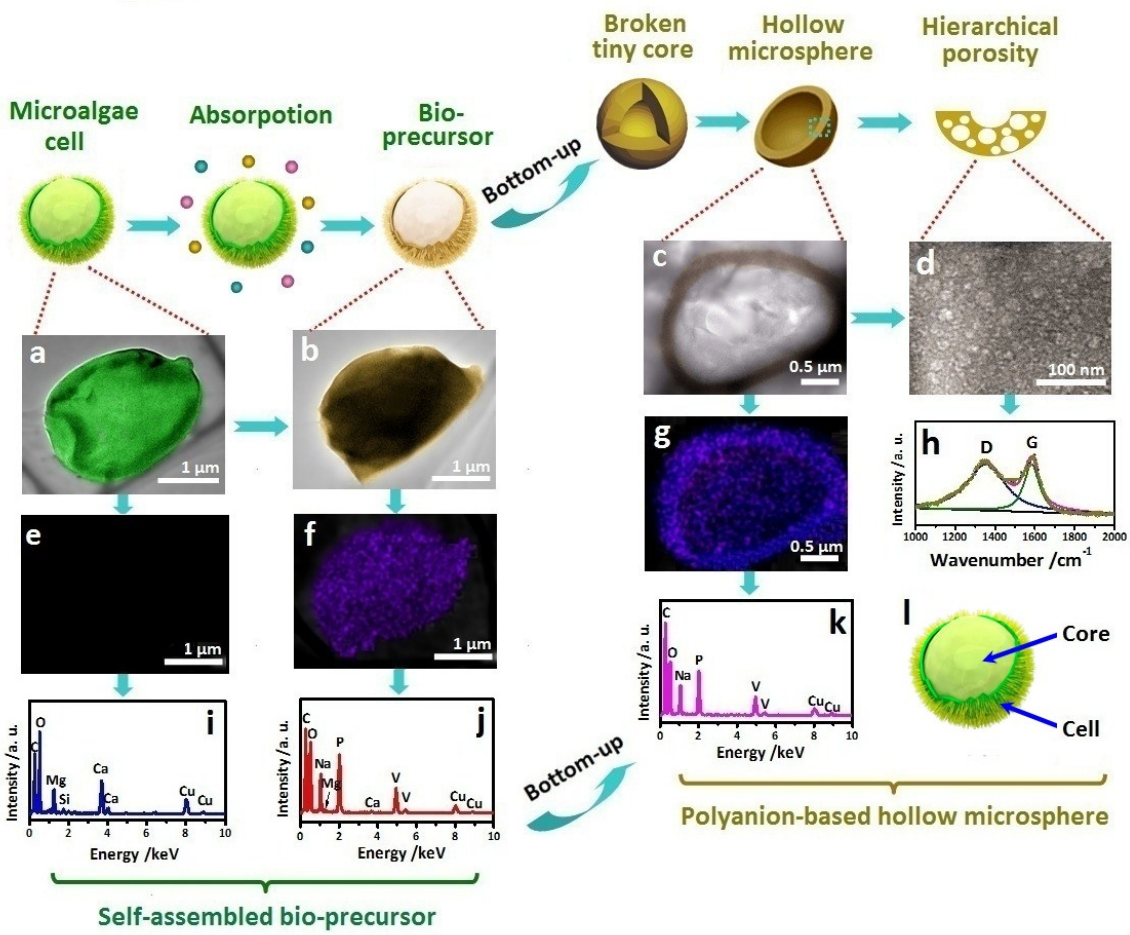


Figure 4 Formation mechanism of polyanion-based hollow porous microspheres: TEM images (a~c), V element mapping (e~g), EDS spectroscopy (i~k) of the microalgae cell (a, e, i), bio-precursor (b, f, j) and hollow porous microsphere (c, g, k). Raman spectroscopy (h) of the bio-directed polyanion-based hollow microsphere. High-resolution TEM (d) of the hierarchical porous shells for the hollow porous microsphere. (i) Schematic illustrations of the structure for a biological microalgae cell. The spheres around the microalgae during biosorption: blue sphere: $Na^{+}$; pink sphere: $V^{3+}$; yellow sphere: $(PO_4)^{3-}$.

process. All these factors result in the hollow porous spherical architecture for the final product. As evidenced by Figure 4c and d, one big hollow in the core and plenty of pores on the shell are constructed in the microsphere. The large *D* than *G* peak in Raman spectroscopy demonstrates the amorphous nature of the carbon-based framework (Figure 4h). The EDS results demonstrate the main elements in the final product are C, Na, P and V. The amounts of impurity elements from the microalgae cell such as Ca, Mg and Si are extreme low and almost undetectable (Figure 4k). The results indicate that trace elements from biological cell have no influence on the composition of final product. Moreover, the uniform vanadium element distribution demonstrates the homogenous composition of the polyanion-based hollow microsphere (Figure 4g).

Based on above results, it comes to the conclusion that the microalgae cell realizes the formation of "bottom" product of spherical bio-precursor, which constructs the "up" product of hollow porous microsphere after calcination. The biochemistry-directed self-assembling process is crucial for the "bottom-up" construction of hollow spherical nanostructure. Moreover, this bio-directed strategy can also be applied in other polyanion-based materials as well. Therefore, the present strategy provides a wide-applicable strategy for the preparation of polyanion-based sodium hosts with tailored architecture.

## 3.4 Sodium intercalation kinetics

The sodium intercalation kinetics of the bio-directed and reference samples are investigated. Firstly, GITT measurements are carried out on all of the samples. Figure 5a and d illustrates the GITT curves and corresponding quasi open-circuit potential (QOCP) curves of the bio-directed samples. For the $Na_3V_2(PO_4)_3$ composites, one pair of plateaus was observed in the charge/discharge QOCP curves. It is associated with the redox reaction of $V^{3+}/V^{4+}$ couple in $Na_3V_2(PO_4)_3$[31]. On the other hand, there are three pairs of plateaus in the charge/discharge curves of $Na_{3.12}Fe_{2.44}(P_2O_7)_2$ composites, which corresponds to a sequence of sodium intercalation steps in the $Fe^{2+}/Fe^{3+}$ redox reaction[32,33].

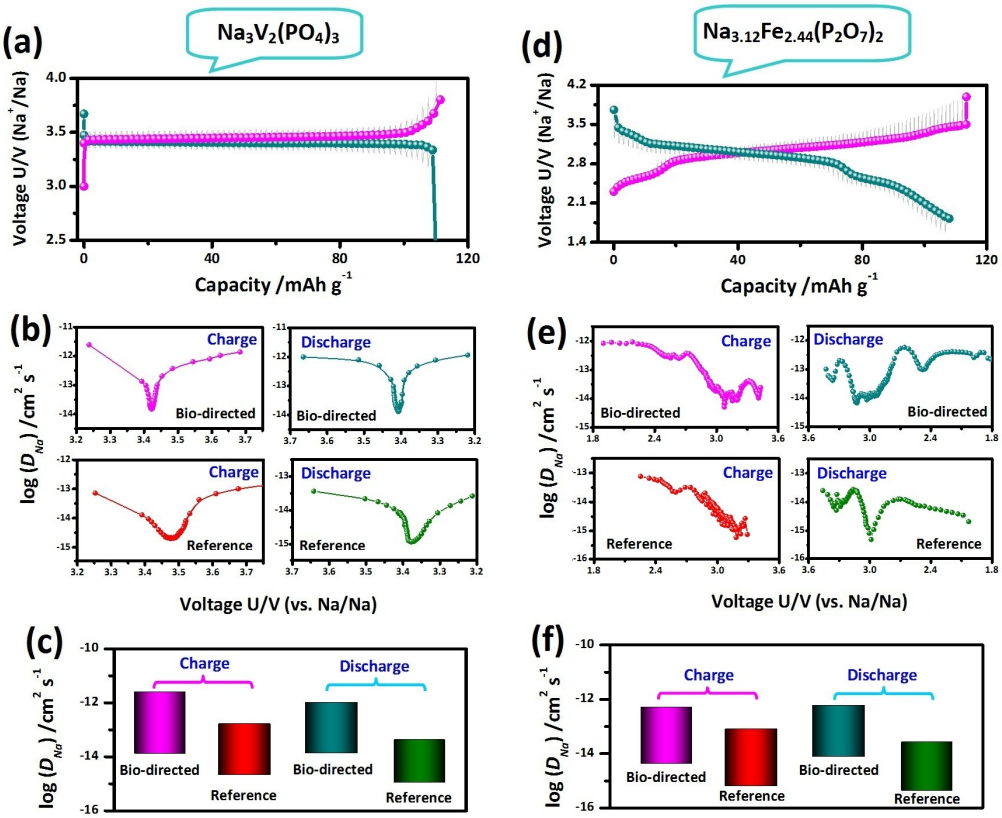


Figure 5 (a, d) GITT and corresponding QOCP curves of the bio-directed samples for $Na_3V_2(PO_4)_3$ (a) and $Na_{3.12}Fe_{2.44}(P_2O_7)_2$ (d) composites. (b, e) Calculated sodium diffusion coefficiencies of the bio-directed and reference samples for the $Na_3V_2(PO_4)_3$ (b) and $Na_{3.12}Fe_{2.44}(P_2O_7)_2$ (e) composites. In b and e, the calculated $D_{Na}$ values in the charge process are displayed in left column and those in the discharge process are displayed in right column. (c, f) Comparisons of the $D_{Na}$ values between the bio-directed and reference samples for the $Na_3V_2(PO_4)_3$ (c) and $Na_{3.12}Fe_{2.44}(P_2O_7)_2$ (f) composites in the charge/discharge process.

The apparent sodium diffusion coefficients ($D_{Na}$) are calculated based on the GITT results according to the Fick's second law (Supplementary S2).

$$D_{Na} = \frac{4}{p}\left(\frac{m_B V_m}{M_B A}\right)^2 \left(\frac{\Delta E_S}{t\left(\frac{dE_t}{d\sqrt{t}}\right)}\right)^2 \qquad (t << L^2/D_{Na}) \quad (1)$$

where $D_{Na}$ ($cm^2\ s^{-1}$) is the sodium diffusion coefficient; $m_B$, $M_B$ and $V_m$ are the mass, molecular weight and molar volume of the electrode material, respectively; A is the interfacial area between electrode and electrolyte; $\tau$ is duration of the current pulse.

In above equation, A represents the contact area between the cathode material and liquid electrolyte. In previous reports, several different methods have been used to calculate its value.[34-40] Firstly, some cases are based on the material's crystallite or grain size, which are derived from the structural or morphological measurements.[34,35] But the uneven sizes of crystallites and/or grains make the determination of A very difficult. Additionally, the electrode comprises PVDF binder and conductive additives, which also affect the real value of A. Secondly, some researchers simplified the calculation process and only used the geometric area of electrode surface as the contact area (A).[36-38] Although such calculation is very simple and convenient, it neglects the different physical characteristics of different active materials and always leads to high errors and misleading results. Finally, a middle case between above two extreme calculations is employed.[39,40] It is based on the specific area of cathode materials, which can be calculated in following equation:

$$A = S \times m \qquad (2)$$

Where S is the BET specific area; m is weight of cathode material in electrode; A is the apparent contact area.

On the one hand, it is a simple and convenient method which avoids some unnecessary and complicated calculation; on the other hand, it also considers the effects of physical characteristics of different cathode materials, and produces more accurate and reliable results. Therefore, we use this strategy to calculate the contact areas (*i.e.* A values) of all the materials in our study.

Figure 5b and e summarize the variation of $D_{Na}$ values as a function of voltage for all the samples. The bio-directed and reference samples of both polyanions exhibit similar trends. In the plateau region, $D_{Na}$ values achieve the minimum value; before and after the plateaus, $D_{Na}$ values increase. Similar phenomena have also been observed in other electrode materials such as $LiFePO_4$, $Li_2FeP_2O_7$, *et al.*[41-43] It can be attributed to the strong interaction between the intercalated cations and the host during ion de/intercalation.[42,43]

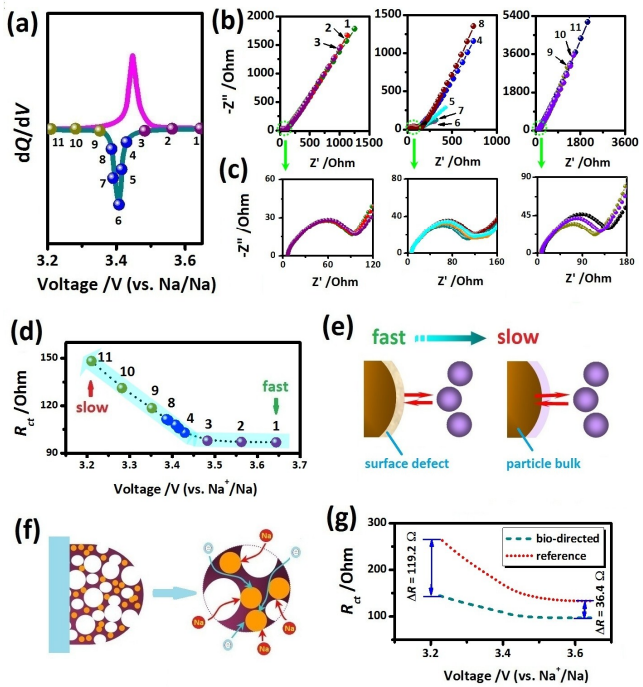


Figure 6 (a) Differential capacity curves of the bio-directed $Na_3V_2(PO_4)_3$ sample. (b) Nyquist plots and (c) enlarged high frequency semicircle. (d) Calculated $R_{ct}$ values at different potentials and (e) schema of the reaction rate during intercalation. (f) Schematic illustration of the fast electron/ion pathways in hierarchical porous architecture. The orange circle represents the nanoscale crystals. (g) Comparison of the $R_{ct}$ values between the bio-directed and reference samples. The difference between the bio-directed and reference samples at beginning and end of the discharge are displayed as inert of g.

On the other hand, for both polyanions, the $D_{Na}$ values of bio-directed samples are much higher than the reference ones in both charge and discharge process. As compared in Figure 5c and f, at least one order higher $D_{Na}$ values are observed for the bio-directed samples than the reference ones. For example, the bio-directed $Na_3V_2(PO_4)_3$ composite achieves the $D_{Na}$ values of $10^{-11.7}$~$10^{-13.9}$ $cm^2\ s^{-1}$ in the charge process, which is higher than the reference one ($10^{-12.8}$~$10^{-14.7}$ $cm^2\ s^{-1}$) by about one order of magnitude. Similarly, the bio-directed $Na_{3.12}Fe_{2.44}(P_2O_7)_2$ sample exhibits the $D_{Na}$ values of $10^{-12.2}$~$10^{-14.1}$ $cm^2\ s^{-1}$ in the discharge process, which is more than one order of magnitude higher than the reference one ($10^{-13.6}$~$10^{-15.4}$ $cm^2\ s^{-1}$).

However, it should be clarified that all the $D_{Na}$ values in our calculation are apparent diffusion coefficients. In fact, the "true" diffusion coefficients are inherent properties of materials and can not be manipulated without creation of defects. In our study, the crystallinity of bioinspired sample is the same as the reference one. Therefore, the "true" diffusion coefficients of both samples should be same. However, the $D_{Na}$ values achieved by GITT calculations in our study are not the "true" inherent diffusion coefficients. Instead, they are "apparent" diffusion coefficients reflecting overall ion diffusivity of the material. Therefore, they can be affected by the contact area of electrolyte-particle and the ion diffusion length. Thus, the higher $D_{Na}$ values of bioinspired samples demonstrate that hollow porous microspherical architecture is beneficial for improving the ion diffusion kinetics for polyanion-based materials.

Next, the electrochemical Impedance Spectroscopy (EIS) is carried out to achieve more detailed information during sodium intercalation. Figure 6a illustrates the differential capacity curves calculated based on the QOCP curves for the bio-directed $Na_3V_2(PO_4)_3$ composite. The redox peaks in these curves correspond to the plateaus in the QOCP curves.[44-47] Figure 6b represents the Nyquist plots recorded at different potentials in the range of 3.65~3.2 V (*vs.* $Na^+$/Na). Based on the different signatures at high, medium, and low frequencies in the spectra, the whole range of potentials can be divided into three stages. When the potentials are in the range of 3.65~3.47 V (point 1~3) and 3.35~3.21 V (point 9~11), the spectra consist of a high-frequency semicircle and a low-frequency straight inclined line. When the potentials are in the range of 3.47~3.35 V (point 4~8), the spectra represent a high-frequency semicircle, a medium-requency arc and a low-frequency straight line. In all the cases, the high-frequency can be attributed to the charge (electron) injection across the interface of the electrode material; and the low-frequency part corresponds to the sodium diffusion process.

The charge transfer resistances ($R_{ct}$) are calculated based on the high frequency part. As displayed in Figure 6d, the $R_{ct}$ values change depending on the electrode potentials. In the beginning of the discharge, the $R_{ct}$ values are almost constant at relative high potentials (3.65~3.47 V, point 1~3). The low $R_{ct}$ values indicate the fast reaction rate at this stage. As discharge proceeds, the electrode potential decreases correspondingly. The continuously increased $R_{ct}$ values in lower potentials (3.47~3.2 V, point 4~11) indicate the decreased reaction rate in deeper discharge. This phenomenon is associated with the surface defects present in the nanostructured materials.[48-50] As schematically illustrated in Figure 6e, the surface defects in the nanoparticles react at a high rate in the early discharge, which results in the lowest charge transfer resistance. These surface defects produce equal electroactive sites on the first atomic layer of the nanoparticles, [48-50] and little variation is observed in the initial $R_{ct}$ values. After the consumption of the surface defects, the bulk of the particle participates and the reaction rate is severely restricted. Therefore, the $R_{ct}$ values dramatically increased in the deep discharge.

On the other hand, the bio-directed samples of both polyanion composites exhibit lower $R_{ct}$ values than the reference ones in the whole potential range (Figure 6g and s4). It suggests the faster rates of surface/bulk reactions for the bio-directed samples than the reference ones. The difference between both samples increase as potential decreases, which demonstrates the superior bulk react capability of bio-directed materials than the reference ones. The results can be attributed to the unique architecture of bio-directed materials. As illustrated in Figure 6f, the nanoscale crystals, hollow porous architecture and 3D conductive framework are favorable to the fast electron/ion transport and superior electrochemical kinetics. Therefore, both

GITT and EIS results confirm that the bio-directed hollow porous microsphere is highly efficient to enhance the sodium intercalation kinetics for polyanion-based materials.

### 3.5 Rate cycling capability

Encouraged by the good sodium intercalation kinetics of bio-directed composites, their electrochemical behaviors are studied. Firstly, the galvanostatic charge-discharge characteristics under different current densities are investigated. The bio-directed samples of both polyanion composites exhibit obvious higher capacities than the reference ones at all current densities. As compared in Figure 7a and e, lower polarization and higher capacities are obtained for both bio-directed samples as compared to those of the reference ones. As the current density increases, the difference between both materials becomes more significant (Figure 7b, f). For example, the bio-directed $Na_3V_2(PO_4)_3$ composite delivers 112 and 89 mAh·g$^{-1}$ of the capacity at the 0.2 *C* and 20 *C* rates, but only 109 (0.2 *C*) and 65 mAh·g$^{-1}$ (20 *C*) are obtained for the reference sample. Similarly, the bio-directed $Na_{3.12}Fe_{2.44}(P_2O_7)_2$ sample composite delivers 104 and 79 mAh·g$^{-1}$ of the capacity at the 0.5 *C* and 5 *C* rates, while only 91 (0.5 *C*) and 56 mAh·g$^{-1}$ (5 *C*) are achieved for the reference sample.

Next, the cycling performances of all the samples are investigated. For both polyanion composites, the bio-directed samples exhibit better cycling property than the reference ones at both low and high rates. As compared in Figure 7(c, g), the bio-directed $Na_3V_2(PO_4)_3$ composite achieves the capacity retentions of 98.1% and 97.1% after cycles at 1 *C* and 10 *C*, which are higher than those of the reference one (94.8% at 1 *C* and 81.2% at 10 *C*). Similarly, the bio-directed $Na_{3.12}Fe_{2.44}(P_2O_7)_2$ sample retains 95.3% (0.5 *C*) and 94.8% (5 *C*) of the initial capacity after cycles, while only 86.1% (0.5 *C*) and 67.4% (5 *C*) of the capacity remained for the reference sample. Moreover, the bio-directed samples are capable of high-rate long-term cycling. As displayed in Figure 7j and k, the bio-directed samples retains 96.2% and 93.1% of the capacity after 500 cycles at high rates of 20 *C* (for $Na_3V_2(PO_4)_3$) and 10 *C* (for $Na_{3.12}Fe_{2.44}(P_2O_7)_2$). The results demonstrate the superior fast charge/discharge capability and long-term cycling stability of the bio-directed samples. To clarify the origin of the superiority of bio-directed composites, the structure and morphology of the samples after cycles are investigated. Figure 7 (d, h) displays the *ex-situ* XRD patterns of the cycled electrodes. For both polyanions, the bio-directed samples exhibit higher peaks intensities than the reference samples, which certifies their improved structural stability and depressed structure deterioration. Moreover, the TEM images of cycled composites (Figure s5) further demonstrate that the morphology of bio-directed samples is maintained after cycling.

Combined above analysis, the superior high-rate long-term cycling property of bio-directed samples can be attributed to their hollow porous spherical architecture. As illustrated in Figure 7i, the 3D carbon framework with hierarchical porosity acts as a

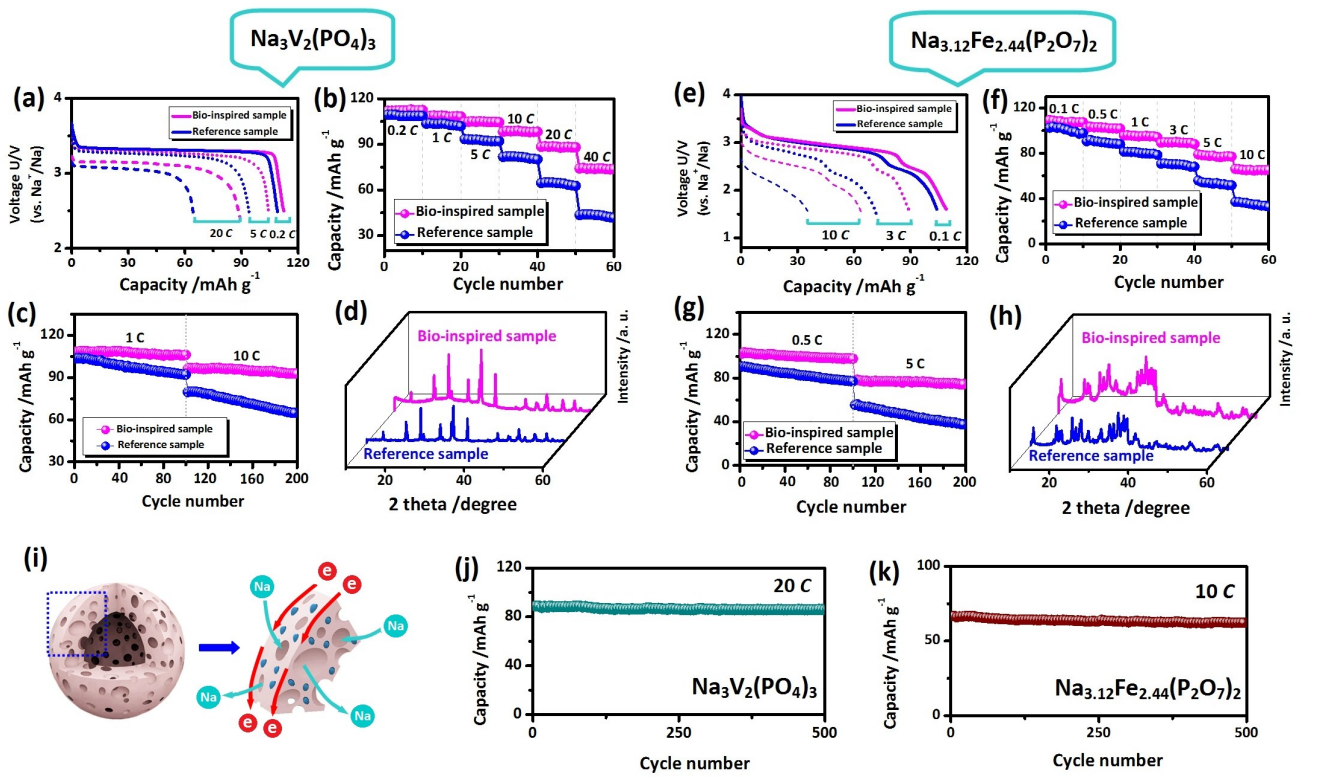


Figure 7 Galvanostatic charge/discharge behaviors of the bio-directed samples: Discharge curves (a, e), rate capability (b, f), cycling property (c, g) and long-term cycling property (j, k) of the bio-directed $Na_3V_2(PO_4)_3$ (a~c, j) and $Na_{3.12}Fe_{2.44}(P_2O_7)_2$ (e~g, k) composites. (d, h) *Ex-situ* XRD patterns of the cycled $Na_3V_2(PO_4)_3$ (d) and $Na_{3.12}Fe_{2.44}(P_2O_7)_2$ (h) materials. (i) Schematic illustration of hollow porous microsphere and the fast electron/ion pathways.

buffer layer for polyanion crystals. It effectively alleviates the volume change during sodium intercalation and enhances the structure stability during long-term cycling. Moreover, the high porous and high conductive framework provides fast electron and ion transport pathways for nanoscale polyanion particles. Therefore, the results demonstrate that constructing bio-directed hollow porous microsphere is a low-cost and highly efficient strategy to realize superb high-rate capability and long-term cycling property for polyanion-based materials in sodium ion batteries.

## 4 Conclusions

In summary, we have reported a biochemistry-directed "bottom-up" approach to construct hollow porous microsphere for polyanion-based sodium hosts. The "bottom" precursor is constructed by the spherical microalgae cell. Its core is tiny and subjected to destroy, while the cell is tough and tends to carbonize during calcination. Both result in the hollow porous microspheres for the "up" product. The polyanion crystals are tightly enwrapped by the high-conductive framework and form the hierarchical nano/microstructure. Taking the advantage of the high porous structure and high conductive framework, the hollow porous microsphere achieves fast electron/ion transport capability and superior sodium intercalation kinetics. As a case study, two kinds of polyanion materials, that is $Na_3V_2(PO_4)_3$ and $Na_{3.12}Fe_{2.44}(P_2O_7)_2$, are employed as target materials. The prepared bio-directed composites achieve desirable electrochemical properties, including superior high rate capability and ultralong-term cycling stability. Therefore, the biochemistry-directed technique is a wide applicable, low-cost and high-efficiency strategy to produce high performance polyanion-based composites for sodium batteries.

## Acknowledgements

This work is supported by the Natural Science Funds for Distinguished Young Scholar of Heilongjiang Province (No. JC2015001), Program for New Century Excellent Talents in Heilongjiang Provincial University (No. 1253-NCET-012) and Natural Science Foundation of Heilongjiang Province (No. QC2013C008).

## Notes and references

[a]*Key Laboratory for Photonic and Electronic Bandgap Materials, Ministry of Education; College of Chemistry and Chemical Engineering, Harbin Normal University, Harbin, 150025, Heilongjiang, China; E-Mail: chaodenghsd@sina.com*

[b]*Key Laboratory of Superlight Material and Surface Technology, Ministry of Education, College of Material Science and Chemical Engineering, Harbin Engineering University, Harbin 150001, Heilongjiang, China; E-Mail: senzhang@hrbeu.edu.cn*

[c]*College of Biological Science and Engineering, Harbin Normal University, Harbin, 150025, Heilongjiang, China*

†Electronic Supplementary Information (ESI) available: Synthesis, morphology and physical characteristics of reference samples; Pore size distribution of the hollow porous microsphere; morphology of the bio-directed $Na_{3.12}Fe_{2.44}(P_2O_7)_2$ hollow microsphere; comparison of the $R_{ct}$ values for the $Na_{3.12}Fe_{2.44}(P_2O_7)_2$ composites; TEM images of the cycled materials; lattice parameters and atomic ratio of the samples; calculation process of sodium intercalation coefficients based on the GITT results. See DOI: 10.1039/b000000x/

1 D. Kundu, E. Talaie, V. Duffort, L. F. Nazar, *Angew. Chem. Int. Ed.* **2015**, *54*, 3431-3448.

2 J. B. Goodenough, K. S. Park, *J. Am. Chem. Soc.* **2013**, *135*, 1167-1176.

3 L. P. Wang, L. H. Yu, X. Wang, M. Srinivasan, Z. J. Xu, *J. Mater. Chem. A* **2015**, *3*, 9353-9378.

4 K. Kubota, S. Komaba, *J. Electrochem. Soc.* **2015**, *162*, A2538-A2550.

5 P. Barpanda, G. Oyama, S. I. Nishimura, S. C. Chung, A. Yamada, *Nat. Commu.* **2014**, *5*, 4358.

6 Y. Meng, T. T. Yu, S. Zhang, C. Deng, *J. Mater. Chem. A* **2016**, *4*, 1624-1631.

7 N. Yabuuchi, K. Kubota, M. Dahbi, S. Komaba, *Chem. Rev.* **2014**, *114*, 11636-11682.

8 C. Deng, S. Zhang, Y. X. Wu, *Nanoscale* **2015**, *7*, 487-491.

9 A. Pan, H. Wu, L. Yu, X. Lou, *Angew. Chem.* **2013**, *125*, 2282-2286.

10 C. Zhang, Z. Chen, Z. Guo, X. Lou, *Energy Environ. Sci.* **2013,** *6,* 974-978.

11 J. Jin, S. Huang, J. Liu, Y. Li, D. Chen, H. Wang, H. Yu, L. Chen, B. Su, *J. Mater. Chem. A* **2014**, *2*, 9699-9708.

12 Y. Ko, S. Park, K. Jung, Y. Kang, *Nano Lett.* **2014**, *13*, 5462-5466.

13 D. Jung, H. Hwang, J. Lee, H. Koo, R. Shakoor, R. Kahraman, Y. Jo, M. Park, J. Choi, *Nano Lett.* **2014**, *14*, 4418-4425.

14 D. Piper, J. Woo, S. Son, S. Kim, K. Oh, S. Lee, *Adv. Mater.* **2014**, *26*, 3520-3525.

15 Y. Wang, Q. Zhu, H. Zhang, *J. Mater. Chem.* **2006**, *16*, 1212-1214.

16 C. L. Chen, N. L. Rosi, *Angew. Chem. Int. Ed.* **2010**, *49*, 1924-1942.

17 Y. P. Zhou, X. H. Rui, W. P. Sun, Z. C. Xu, Y. Zhou, W. J. Ng, Q. Y. Yan, E. Fong, *ACS Nano*, **2015**, *9*, 4628-4635.

18 C. K. Jeong, I. Kim, K. Park, H. Paik, G. T. Hwang, K. No, Y. S. Nam, K. J. Lee, *ACS Nano*, **2013**, *7*, 11016-11025.

19 M. Moradi, Z. Li, J. F. Qi, W. T. Xing, K. Xiang, Y. M. Chiang, A. M. Belcher, *Nano Lett.* **2015**, *15*, 2917-2921.

20 E. R. Pinero, M. Cadek, F. Beguin, *Adv. Funct. Mater.* **2009**, *19*, 1032-1039.

21 C. X. Lv, X. F. Yang, A. Umar, Y. Z. Xia, Y. Jia, L. Shang, T. Zhang, D. J. Yang, *J. Mater. Chem. A* **2015**, *3*, 22708-22715.

22 Y. Xia, Z. Xiao, X. Dou, H. Huang, X. H. Lu, R. J. Yan , Y. P. Gan, W. J. Zhu, J. P. Tu, W. K. Zhang, X. Y. Tao, *ACS Nano*, **2013**, *7*, 7083-7092.

23 T. J. Zhang, W. Wang, D. Y. Zhang, X. X. Zhang, Y. R. Ma, Y. L. Zhou, L. M. Qi, *Adv. Funct. Mater.* **2010**, *20*, 1152-1160.

24 D. Y. Chung, K. J. Lee, S. H. Yu, M. Kim, S. Y. Lee, O. H. Kim, H. J. Park, Y. E. Sung, *Adv. Energy Mater.* **2015**, *5*, 1401309.

25 X. Y. Tao, R. Wu, Y. Xia, H. Huang, W. C. Chai, T. Feng, Y. P. Gan, W. K. Zhang, *ACS Appl. Mater. Interfaces* **2014**, *6*, 3696-3702.

26 Y. Xia, W. K. Zhang, H. Huang, Y. P. Gan, Z. Xiao, L. C. Qian, X. Y. Tao, *J. Mater. Chem.* **2011**, *21*, 6498-6501.

27 Y. Zhou, X. Rui, W. Sun, Z. Xu, Y. Zhou, W. J. Ng, Q. Yan, E. Fong, *ACS Nano*, **2015**, *9*, 4628-4635.

28 M. K. Lam, K. T. Lee, *Biotechnol. Adv.* **2012**, *30*, 673-690.

29 H. J. Cho, K. Baek, J. K. Jeon, S. H. Park, D. J. Suh, Y. K. Park, *Chem. Eng. J.* **2013**, *217*, 205-211.

30 Y. P. Kumar, P. King, V. S. R. K. Prasad, *Chem. Eng. J.* **2007**, *129*, 161-166.

31 Q. Y. Wang, B. D. Zhao, S. Zhang, X. H. Gao, C. Deng, *J. Mater. Chem. A* **2015**, *3*, 7732-7740.

32 Y. B. Niu, M. W. Xu, C. J. Cheng, S. J. Bao, J. K. Hou, S. G. Liu, F. L. Yi, H. He, C. M. Li, *J. Mater. Chem. A* **2015**, *3*, 17224-17229.

33 B. Lin, S. Zhang, C. Deng, *J. Mater. Chem. A* **2016**, *4*, 2550-2559.

34 W. Weppner, R. A. Huggins, *J. Electrochem. Soc.* **1977**, *124*, 1569-1575.

35 D. Baster, K. Zheng, W. Zajac, K. Swierczek, J. Molenda, *Electrochim. Acta*, **2013**, *92*, 79-86.

36 S. Yang, X. Wang, X. Yang, Y. Bai, Z. Liu, H. Shu, Q. Wei, *Electrochim. Acta*, **2012**, *66*, 88-93.

37 J. Hong, C. S. Wang, U. Kasavajjula, *J. Power Sources*, **2006**, *162*, 1289-1296.

38 H. Gao, S. Zhang, C. Deng, *Dalton Trans.* **2015**, *44*, 138-145.

39 K. M. Shaju, G. V. S. Rao, B. V. R. Chowdari, *J. Electrochem. Soc.* **2004**, *151*, A1324-A1332.

40 Y. J. Zhu, Y. H. Xu, Y. H. Liu, C. Luo, C. S. Wang, *Nanoscale*, **2013**, *5*, 780-787.

41 L. Tan, S. Zhang, C. Deng, *J. Power Sources* **2015**, *275*, 6-13.

42 K. Tang, X. Yu, J. Sun, H. Li, X. Huang, *Electrochim. Acta*, **2011**, *56*, 4869-4875.

43 X. Rui, N. Ding, J. Liu, C. Li, C. Chen, *Electrochim. Acta*, **2010**, *55*, 2387-2390.

44 C. Deng, S. Zhang, B. L. Fu, S. Y. Yang, L. Ma, *J. Alloys Compd.* **2010**, *496*, 521-527.

45 S. Zhang, C. Deng, S. Y. Yang, L. Ma, *J. Alloys Compd.* **2009**, *484*, 519-523.

46 S. Y. Yang, S. Zhang, B. L. Fu, Q. Wu, F. L. Liu, C. Deng, *J. Solid State Electrochem.* **2011**, *15*, 2633-2638.

47 S. Zhang, C. Deng, H. Gao, F. L. Meng, M. Zhang, *Electrochim. Acta* **2013**, *107*, 406-412.

48 H. Heli, H. Yadegari, A. Jabbari, *J. Phys. Chem. C.* **2011**, *115*, 10889-10897.

49 M. Quintin, O. Devos, M. H. Delville, G. Campet, *Electrochim. Acta* **2006**, *51*, 6426-6434.

50 B. D. Zhao, B. Lin, S. Zhang, C. Deng, *Nanoscale* **2015**, *7*, 18552-18560.